Advances in Geo-Energy Research

Vol. 18, No. 2, p. 137-152, 2025

Original article

Quantum machine learning-driven surrogate modeling for efficient multi-objective optimization of CO_2 storage and geothermal energy extraction

Babak Mohammadi[1], Mingjie Chen[2]*, Mohammad Reza Nikoo[3], Ali Al-Maktoumi[2]

[1]*Hydrology Research Unit, Swedish Meteorological and Hydrological Institute, Norrköping 601 76, Sweden*

[2]*Water Research Center, Sultan Qaboos University, Muscat 123, Oman*

[3]*Department of Civil and Architectural Engineering, Sultan Qaboos University, Muscat 123, Oman*

Keywords:
CO_2 plume geothermal systems
quantum machine learning
multi-objective optimization
surrogate modeling
carbon sequestration

Cited as:
Mohammadi, B., Chen, M., Nikoo, M. R., Al-Maktoumi, A. Quantum machine learning-driven surrogate modeling for efficient multi-objective optimization of CO_2 storage and geothermal energy extraction. Advances in Geo-Energy Research, 2025, 18(2): 137-152. https://doi.org/10.46690/ager.2025.11.04

Abstract:
CO_2 plume geothermal systems offer a promising pathway for simultaneous carbon sequestration and renewable energy production, yet their optimization remains computationally prohibitive due to the complexity of coupled multi-phase flow, heat transport, and thermodynamic processes. This study presents a novel framework that integrates Non-isothermal Unsaturated-saturated Flow and Transport modeling with quantum neural network and hybrid quantum-classical ensemble regressors to accelerate CO_2 plume geothermal system design optimization. The methodology employs latin hypercube sampling to generate 1,000 Non-isothermal Unsaturated-saturated Flow and Transport simulations across several parameter spaces, extracting statistical features that undergo rigorous selection through Boruta, Chi-squared, and Pearson correlation algorithms with a standardized weight threshold of higher than 0.75. Two quantum architectures were developed to predict six geothermal variables, including system lifetime, injected, extracted, stored CO_2 mass, cumulative energy recovery and average heat extraction rate within lifetime. The quantum models achieved exceptional accuracy for most variables in the test section, with hybrid quantum-classical ensemble regressors architectures consistently outperforming quantum neural network variants, particularly when combined with boruta feature selection. Two optimization algorithms were employed for CO_2 plume geothermal system design, including moth flame optimization for single objectives and non-dominated sorting genetic algorithm II for multi-objective scenarios to find robust optimal solutions based on developed surrogate models for injection overpressure, well spacing near and maximizing thermal energy extraction. The framework transformed a computationally intractable optimization requiring extensive simulation time into a rapid calculation while maintaining prediction accuracy comparable to full-physics models.

1. Introduction

The urgent need to mitigate climate change while meeting growing global energy demands has intensified the search for innovative technologies that can simultaneously address carbon emissions and renewable energy production (Metz et al., 2005). Traditional carbon capture and storage technologies, while technically proven, face significant economic barriers due to high operational costs and the absence of direct revenue generation, necessitating novel approaches that can transform CO_2 sequestration from a costly burden into an economically viable opportunity (Mac et al., 2017; Bui et al., 2018). As a

Yandy Scientific Press

*Corresponding author.
E-mail address: babak.mohammadi@smhi.se (B. Mohammadi); mingjie@squ.edu.om (M. Chen); m.reza@squ.edu.om (M. Nikoo); ali4530@squ.edu.om (A. Al-Maktoumi).

Received August 26, 2025; revised September 19, 2025; accepted October 8, 2025; available online October 11, 2025.

carbon capture, utilization, and storage approach, CO_2 plume geothermal (CPG) systems have emerged as a promising technology that re-conceptualizes injected CO_2 not merely as waste to be stored, but as a valuable working fluid that can extract geothermal energy from sedimentary basins and depleted hydrocarbon reservoirs previously considered unsuitable for conventional geothermal development (Randolph and Saar, 2011; Chen et al., 2021). CPG systems generally achieve higher power generation efficiency than water-based geothermal systems, especially in low-permeability or low-temperature reservoirs, due to CO_2's superior thermophysical properties. CO_2 has lower viscosity than water, indicating higher mobility during migration in porous reservoir formations. Particularly, the significant thermosiphon effect during CO_2-circulated geothermal extraction can achieve pump-free cycle, saving tremendous power consumption in tradition water-based geothermal harvest (Norouzi et al., 2022; Zhong et al., 2023; Antoneas and Koronaki, 2024). The unique thermophysical properties of supercritical CO_2, particularly its lower viscosity compared to water, higher mobility, and substantial compressibility which can enable more efficient heat extraction through enhanced buoyancy-driven circulation and improved reservoir sweep efficiency, while the injected CO_2 remains permanently sequestered through multiple trapping mechanisms including structural, residual, solubility, and mineral trapping (Fleming et al., 2018; Ezekiel et al., 2020; Rajabi et al., 2021). This dual-benefit approach fundamentally transforms the economics of both carbon sequestration and geothermal energy by creating a synergistic system where revenues from renewable electricity generation can offset carbon capture and storage costs, potentially enabling widespread deployment of carbon-negative baseload power generation that addresses both climate mitigation and energy security challenges simultaneously (Buscheck et al., 2016; Chen et al., 2022; Titus et al., 2023; Loschetter et al., 2025).

The numerical modeling of CPG systems presents formidable computational challenges arising from the complex interplay of coupled non-isothermal multi-phase flow, multicomponent transport, thermodynamic phase transitions, and geochemical reactions that must be resolved across multiple spatial and temporal scales (Pruess, 2008). High-fidelity simulators such as Non-isothermal Unsaturated-saturated Flow and Transport (NUFT) require solving large systems of highly nonlinear partial differential equations, where even a single forward simulation of a field-scale CPG reservoir over its operational lifetime can demand days or weeks of computational time on high-performance computing clusters, making comprehensive optimization studies computationally prohibitive (Buscheck et al., 2012; Chen et al., 2021). This computational burden becomes particularly acute when conducting robust uncertainty quantification and optimization studies, where thousands of simulations are typically required to explore parameter spaces, evaluate different well configurations, and assess geological uncertainties, transforming what should be routine design tasks into computationally intractable problems that can require months of continuous computation (Dai et al., 2014; Rajabi et al., 2021). The situation is further complicated by the need to capture critical phenomena such as thermal breakthrough, viscous fingering, gravity override, and convective mixing, which require fine spatial discretization and small-time steps to resolve accurately, yet doing so exponentially increases computational demands (Garapati et al., 2015; Williams and Chadwick, 2021). Researchers face an inherent trade-off between model fidelity and computational tractability: simplified analytical or reduced-order models enable rapid calculations but may miss crucial physics that govern system performance, while high-fidelity numerical models capture complex phenomena but require computational resources that exceed practical limits for iterative design optimization and real-time reservoir management (Norouzi et al., 2021; Wen et al., 2021; Rajabi et al., 2022). This computational bottleneck has emerged as a critical barrier preventing the widespread deployment and optimization of CPG technology, as operators require rapid design tools and adaptive management strategies that current numerical modeling frameworks cannot provide within reasonable timeframes or computational budgets.

Surrogate modeling approaches for geothermal systems have undergone significant evolution from simple methods to sophisticated machine learning (ML) architectures, demonstrating substantial computational speedup while maintaining acceptable accuracy for production forecasting and optimization tasks (Wang et al., 2022; Ye et al., 2024; Li et al., 2025). Classical ML algorithms, including random forests, support vector machines, and artificial neural networks, have been successfully deployed for various reservoir modeling applications such as permeability field reconstruction, thermal breakthrough prediction, and well placement optimization, with deep learning models particularly excelling at capturing spatiotemporal patterns in pressure and temperature fields from limited observation data (Nikravesh et al., 2001; Teixeira and Secchi, 2019; Saikia et al., 2020; Ng et al., 2023). However, conventional ML models face fundamental limitations in extrapolating beyond their training domains and struggle to preserve critical physical constraints (Malik, 2020; Shen et al., 2023), such as mass conservation, energy balance, and thermodynamic consistency, leading to non-physical predictions when operating conditions deviate significantly from training scenarios. The inherent accuracy-efficiency paradox manifests prominently in current surrogate models: physics-informed neural networks that incorporate governing equations achieve higher fidelity but require substantially longer training times and struggle with convergence for strongly coupled multiphysics problems, while purely data-driven models train rapidly but exhibit poor generalization for complex phase transition regions and near-critical fluid states (Fraces and Tchelepi, 2021; Zhou et al., 2022; Semler and Weiser, 2023; Chen, 2024).

Previous studies have successfully demonstrated the application of data-driven methods for CPG system optimization and prediction with bagging multivariate adaptive regression splines and artificial neural networks approaches in North Oman reservoirs (Rajabi et al., 2022; Chen et al., 2023). However, while these classical ML approaches provide substantial computational acceleration, they face inherent limitations in capturing the full complexity of multi-phase flow dynamics, particularly the intricate phase transitions, thermodynamic

interactions, and nonlinear coupling between CO_2 properties and heat transport that govern CPG system performance. Furthermore, existing studies typically apply ML models directly without systematic feature engineering or rigorous selection of predictive variables, potentially missing critical relationships and introducing noise that compromises model accuracy and generalization. Although ML techniques have been widely applied across reservoir engineering, quantum machine learning (QML) has received little attention in the context of geothermal energy, and its application to CPG systems presents a novel opportunity for advancing surrogate modeling and optimization. This gap presents an opportunity for QML frameworks that combine comprehensive feature selection methodologies with quantum-inspired pattern recognition capabilities, leveraging quantum gate operations and entanglement to create nonlinear feature transformations and capture subtle correlations for enhanced surrogate modeling of complex CPG systems.

This research presents novel quantum-based ML frameworks that combine both feature engineering and quantum computing capabilities to overcome the computational barriers limiting CPG system optimization, with the primary objective of developing an efficient QML-based surrogate model that achieves high accuracy while dramatically reducing computational time compared to traditional NUFT simulations. The proposed integration methodology establishes a novel surrogate model to combine NUFT and QML hybrid framework where high-fidelity NUFT simulations generate training data for quantum neural network (QNN) and hybrid quantum-classical ensemble regressors. In addition, quantum-scaled feature encoding and three comparative feature selection algorithms (Boruta, Chi-squared filter, and Pearson correlation) systematically identifying optimal input parameters for predicting critical performance metrics including system lifetime (tLife), injected CO_2 within lifetime (iCO_2), extracted CO_2 within lifetime (eCO_2), stored CO_2 within lifetime (sCO_2), cumulative energy recovered in lifetime (extEn), and heat extraction rate averaged over the lifetime (extQh). Therefore the current study seeks: (1) the pioneering application of QML to CPG system optimization, demonstrating quantum advantage in capturing the nonlinear, multi-scale physics of coupled CO_2-heat-flow processes; (2) a comprehensive comparative analysis of feature selection methodologies, revealing that quantum-enhanced feature spaces achieve superior performance in identifying critical parameters; (3) applying a novel hybrid optimization framework based on a developed surrogate model utilizing moth flame optimization (MFO) for single-objective scenarios and non-dominated sorting genetic algorithm II (NSGA-II) for multi-objective problems to maximize thermal energy.

2. Methodology

2.1 Data preparation and framework design

The NUFT code v2.0 is employed as the primary numerical simulator for modeling coupled CO_2-brine multi-phase flow and heat transport in the geothermal reservoir system. In this study, the three-dimensional computational domain represents a fault-bounded reservoir block in North Oman (Chen et al., 2023). More detailed information regarding the NUFT model framework and spatial discretization is provided in Supplementary A of the supplementary information , and information about the initial conditions and simulation scenarios is provided in Supplementary B of the supplementary information. A comprehensive dataset was generated using latin hypercube sampling to systematically explore the seven-dimensional parameter space encompassing both operational decision variables and geostatistical parameters controlling reservoir heterogeneity. The latin hypercube sampling approach generated 100 quasi-random samples ensuring uniform coverage across the parameter ranges: injection well overpressure (5-15 MPa), well spacing (400-1,000 m), porosity variance (0.001-0.004), azimuth angle (0-45°), and correlation lengths in X, Y, and Z directions (100-1,000 m, 100-1,000 m, and 1-20 m, respectively). For each parameter combination, 10 equally probable realizations of the spatially correlated porosity-permeability fields were generated using sequential gaussian simulation, resulting in 1,000 unique reservoir models that capture geological uncertainty while maintaining computational feasibility. Each NUFT simulation produces four primary output files recorded at hourly timesteps over the operational lifetime: (1) CO_2 mass rate injected, (2) CO_2 mass rate produced, (3) average temperature of produced fluid (°C), and (4) produced heat flux (MW).

Six performance indicators were derived from the raw NUFT simulation outputs to comprehensively characterize CPG system performance across thermal, storage, and operational dimensions. The target variables (explained in Table 1) include tLife, iCO_2, eCO_2, sCO_2, extEn, and extQh. To capture the temporal dynamics and reduce dimensionality for ML applications, four statistical features were extracted from each time-series output of CI, CP, CPQ, and CPT, including mean, range (maximum-minimum), standard deviation, and median values, transforming the high-dimensional temporal data into a tractable feature vector. The statistical features were computed for each of the 10 realizations per sample and subsequently averaged to obtain 100 representative feature vectors, creating a robust dataset where each sample encapsulates both the central tendency and variability of system behavior. Then these variables, together with decision variables (Dp and Lw) and geostatistical parameters (Var, Az, CLx, Cly, CLz), were considered as input of ML models. Table 1 presents all input parameters and output variables used in the CPG system modeling in the current study.

Fig. 1 shows the developed framework of the current study. The proposed framework consists of four interconnected phases: numerical simulation using NUFT modeling to generate comprehensive datasets from decision variables, including injection well overpressure and well spacing parameters, followed by a feature selection phase employing the Boruta algorithm, Chi-squared filter, and Pearson correlation analysis to identify the most influential parameters. The selected features undergo preprocessing through power transform, principal component analysis , and quantum scaling to create quantum-ready inputs for surrogate model development using both QNN and HQER to predict key geothermal

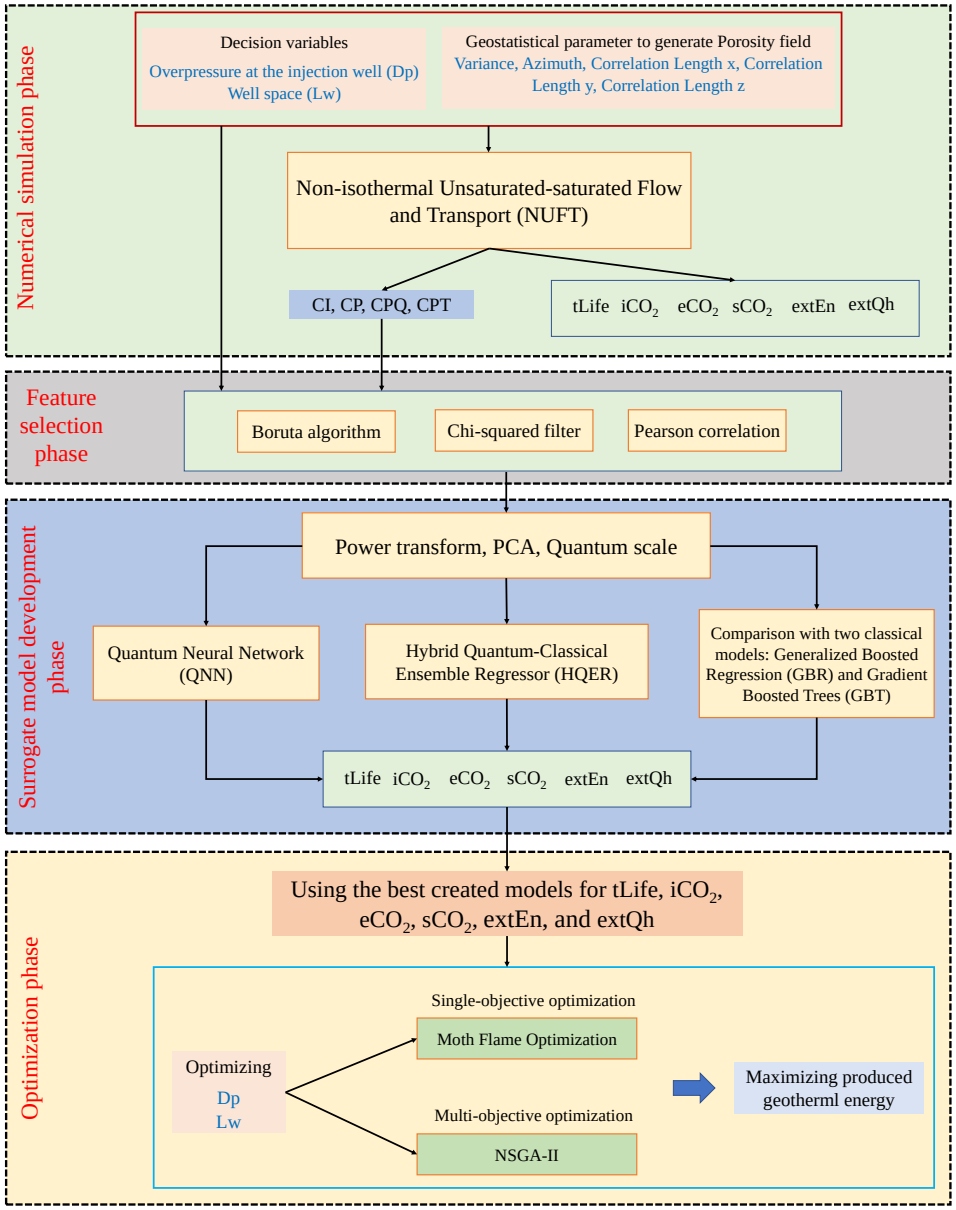

Fig. 1. Comprehensive quantum-enhanced framework for geothermal energy optimization integrating numerical simulation, feature selection, QML surrogate modeling, and multi-objective optimization for maximizing geothermal energy production.

parameters, including CO_2 lifetime and extraction efficiency. The final optimization phase implements both single-objective MFO and multi-objective NSGA-II algorithms to maximize produced geothermal energy while optimizing injection well operational parameters, demonstrating the integration of QML with traditional optimization techniques for enhanced geothermal system performance. The feature selection algorithms, quantum machine learning models, and classical baseline development are described in Supplementary B of the supplementary information.

2.2 Optimization frameworks via single and multi-objective optimization approaches

The optimization framework employs the best-performing developed QML models, where each of the six target variables (tLife, iCO_2, eCO_2, sCO_2, extEn, extQh) was independently predicted using QNN or HQER models under various feature selection scenarios (Boruta, Chi-squared, Pearson correlation). The best model for each target variable was identified based on test set performance metrics. The optimization framework implements two optimization algorithms tailored to the problem dimensionality; including MFO for single-objective scenarios and NSGA-II for multi-objective problems.

The MFO algorithm (Mirjalili, 2015), a nature-inspired metaheuristic based on the transverse orientation navigation behavior of moths, was employed in this study. The optimization process utilized a population of 40 moths evolving over 300 iterations, where each moth's position denoted a candidate solution and flames represented the best solutions obtained. Position updates were governed by a logarithmic spiral mech-

Table 1. Summary of input parameters, NUFT simulation outputs, and target variables used in the developed QML framework for CPG system optimization.

Model	ID	Parameters	Unit
Decision variables	Dp	Overpressure at the injection well	MPa
	Lw	Well space	m
Geostatistical parameters to generate a porosity field	Var	Variance	/
	Az	Azimuth	°
	CLx	Correlation Length x	m
	CLy	Correlation Length y	m
	CLz	Correlation Length z	m
NUFT flow model	CI	CO_2 mass rate injected	kg/s
	CP	CO_2 mass rate produced	kg/s
	CPQ	Produced heat flux in MW	Mega Watts: 10^6 Joule/second
	CPT	Average temperature of produced fluid	°C
Target variables	tLife	Years until production well drops below 80 °C	Year
	iCO_2	Injected CO_2 within lifetime	Mt
	eCO_2	Extracted CO_2 within lifetime	Mt
	sCO_2	Stored CO_2 within lifetime	Mt
	extEn	Cumulative energy recovered in lifetime	10^{15} J (PJ)
	extQh	Heat extraction rate averaged in lifetime	MW

anism. For multi-objective optimization, the NSGA-II was used to perform multi-objective optimization. The algorithm was configured with a population size of 40, 300 generations, a tournament size of 2, a crossover probability of 0.7 with a distribution index of 5, and a mutation probability of 0.2 with a distribution index of 10. This configuration enabled the exploration of the Pareto front, capturing the optimal trade-offs among conflicting objectives. The optimization algorithm parameters were selected based on established guidelines from prior studies and preliminary convergence tests to ensure a balance between computational tractability and convergence reliability. Six distinct optimization scenarios were developed to investigate different trade-offs in the design of the CPG system. Each scenario targeted a unique combination of objectives, as listed in Table 2, ranging from maximizing a single objective to simultaneously optimizing multiple objectives. Details of the model accuracy assessment metrics, including the mean absolute error (MAE), root mean square error (RMSE), relative error expressed as the RMSE–standard deviation ratio (RSR), refined index of agreement (d*r*), and the coefficient of determination (R^2), are provided in Supplementary C of the supplementary information.

3. Results and discussion

3.1 Feature selection

The application of three distinct feature selection algorithms revealed significant variability in the identified critical predictors for each target variable, demonstrating the complex, nonlinear relationships between NUFT simulation outputs and CPG system performance metrics (Table 3). The BO consistently identified compact feature sets emphasizing temperature statistics (CPT_mean, CPT_median) for tLife and Lw_m and Az_deg combined with CPT_mean for iCO_2, eCO_2, sCO_2, and extEn, while selecting a broader set of features including CP_range, CPQ_range, CP_mean, CP_median, CP_sd, CPQ_mean, CI_median, CI_mean, CPQ_median for extQh. CH method exhibited Lw_m and Az_deg as effective variables for iCO_2, eCO_2, sCO_2, and extEn, while it suggested more effective variables for extQh. In contrast, PC systematically selected the largest feature sets, particularly for tLife (15 features) and extQh (15 features), capturing correlations through comprehensive inclusion of CI, CP, CPT, and CPQ statistics along with Lw_m, Az_deg, and dP_MPa. The consistent appearance of well Lw_m and Az_deg across all CO_2-related outputs (iCO_2, eCO_2, sCO_2, extEn) underscores their fundamental role in controlling CO_2 plume migration and storage dynamics, while the dominance of production statistics (CP_range, CPQ_range, CP_mean) for extQh reflects the direct physical relationship between fluid production and thermal energy recovery. The information presented in Table 4 served as the input variables for the QNN and HQER models, which were compared with two widely used classical ML algorithms, namely generalized boosted regression (GBR) and gradient boosted trees (GBT). Details of the GBR and GBT

Table 2. Optimization scenarios formulated for CPG system design, highlighting different combinations of objectives and corresponding optimization rounds. Note: "max" denotes maximization of the corresponding objective, while "min" denotes minimization.

Scenario No.	Objective(s)	Round
1	extEn	Max extEn
2	extEn, extQh	Max extEn + max extQh
3	extEn, extQh, tLife	Max extEn + max extQh + max tLife
4	extEn, sCO_2	Max extEn + max sCO_2
5	extEn, sCO_2, iCO_2	Max extEn + max sCO_2 + min iCO_2
6	extEn, sCO_2, iCO_2, extQh, tLife	Max extEn + max sCO_2 + min iCO_2 + max extQh + max tLife

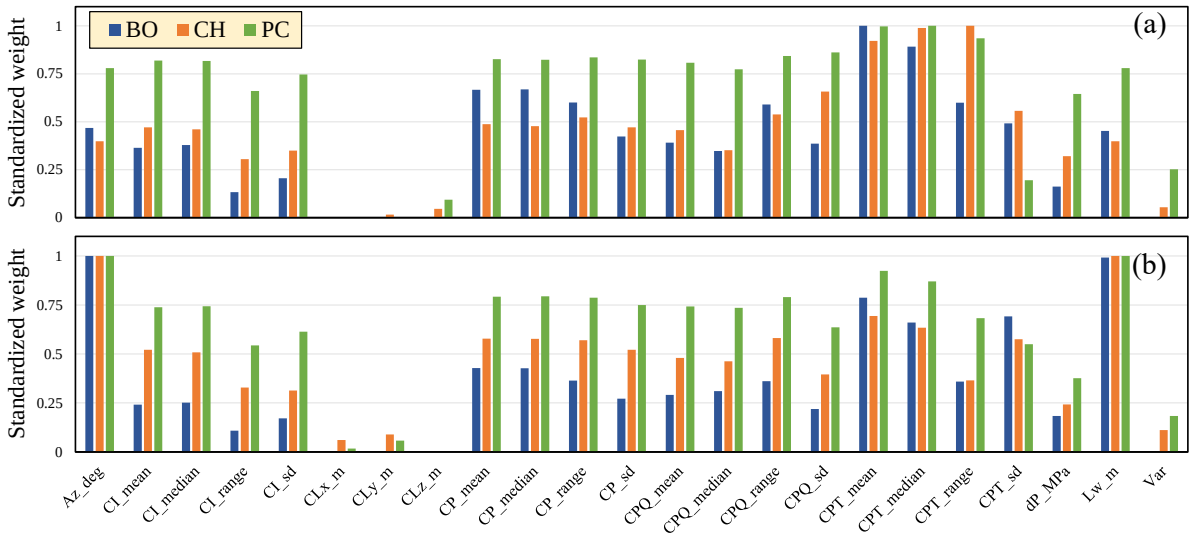

Fig. 2. Standardized feature importance weights (0-1 scale) for tLife (a) and extEn (b) across three feature selection methods.

models are provided in Supplementary B of the supplementary information.

The standardized feature importance weights across the three selection algorithms reveal distinct patterns in how different statistical measures influence each target variable, with notable variations in both the magnitude and consistency of feature contributions (Fig. 2 and Fig. D1 of Supplementary D in the supplementary information). For system lifetime (tLife), temperature-related features (CPT_mean, CPT_median, CPT_range) consistently achieve high importance weights across all three methods, particularly under PC, which assigns weights exceeding 0.90, confirming temperature as the primary driver of operational longevity. The CO_2 mass balance variables (iCO_2, eCO_2, sCO_2) exhibit remarkably similar feature importance profiles, with geometric parameters (Lw_m, Az_deg) demonstrating uniformly high weights (> 0.75) across all selection methods, while production and injection statistics show method-dependent importance, Boruta and Chi-squared assign minimal weights to most flow statistics, whereas PC method identifies moderate importance (0.50-0.75) for production metrics (CP_mean, CP_range). Thermal energy extraction (extEn) displays a pattern nearly identical to the CO_2 storage variables, reinforcing the coupled nature of heat extraction and CO_2 circulation, with well spacing emerging as the dominant predictor (standardized weight > 0.95) under all methods. In contrast, heat extraction rate (extQh) shows a fundamentally different importance distribution, where production and heat flux statistics (CP_range, CPQ_range, CP_mean, CPQ_mean) consistently achieve high weights (> 0.75) across all methods, while geometric parameters that dominate other outputs show relatively low importance (< 0.50), highlighting the direct dependence of instantaneous heat flux on current production conditions rather than well configuration. The threshold application effectively filtered out marginally relevant features, reducing the average feature set size from 20 potential predictors to 3-15 selected features depending on the method and target variable, with Chi-squared consistently producing the most parsimonious selections and PC method retaining the most comprehensive feature sets.

3.2 Surrogate modeling performance

The surrogate QML models for tLife prediction demonstrate strong performance across both architectures in Table 4, with HQER models generally outperforming QNN counterparts during training while showing more heterogeneous

Table 3. Selected features for each target variable using three feature selection algorithms and their corresponding QML and classical model names.

No.	Feature selection method	Input(s)	Output	Model			
1	Boruta algorithm	CPT_mean, CPT_median	tLife	BO-QNN1	BO-HQER1	BO-GBR1	BO-GBT1
2	Chi-squared filter	CPT_range, CPT_median, CPT_mean	tLife	CH-QNN1	CH-HQER1	CH-GBR1	CH-GBT1
3	Pearson correlation	CPT_median, CPT_mean, CPT_range, CPQ_sd, CPQ_range, CP_range, CP_mean, CP_sd, CP_median, CI_mean, CI_median, CPQ_mean, Lw_m, Az_deg, CPQ_median	tLife	PC-QNN1	PC-HQER1	PC-GBR1	PC-GBT1
4	Boruta algorithm	Lw_m, Az_deg, CPT_mean	iCO_2	BO-QNN2	BO-HQER2	BO-GBR2	BO-GBT2
5	Chi-squared filter	Lw_m, Az_deg	iCO_2	CH-QNN2	CH-HQER2	CH-GBR2	CH-GBT2
6	Pearson correlation	Az_deg, Lw_m, CPT_mean, CPT_median, CP_median, CP_mean, CPQ_range, CP_range	iCO_2	PC-QNN2	PC-HQER2	PC-GBR2	PC-GBT2
7	Boruta algorithm	Az_deg, Lw_m, CPT_mean	eCO_2	BO-QNN3	BO-HQER3	BO-GBR3	BO-GBT3
8	Chi-squared filter	Lw_m, Az_deg	eCO_2	CH-QNN3	CH-HQER3	CH-GBR3	CH-GBT3
9	Pearson correlation	Lw_m, Az_deg, CPT_mean, CPT_median, CP_median, CP_mean, CPQ_range, CP_range	eCO_2	PC-QNN3	PC-HQER3	PC-GBR3	PC-GBT3
10	Boruta algorithm	Az_deg, Lw_m, CPT_mean	sCO_2	BO-QNN4	BO-HQER4	BO-GBR4	BO-GBT4
11	Chi-squared filter	Lw_m, Az_deg	sCO_2	CH-QNN4	CH-HQER4	CH-GBR4	CH-GBT4
12	Pearson correlation	Az_deg, Lw_m, CPT_mean, CPT_median, CP_median, CPQ_range, CP_mean, CPT_range, CP_range	sCO_2	PC-QNN4	PC-HQER4	PC-GBR4	PC-GBT4
13	Boruta algorithm	Az_deg, Lw_m, CPT_mean	extEn	BO-QNN5	BO-HQER5	BO-GBR5	BO-GBT5
14	Chi-squared filter	Lw_m, Az_deg	extEn	CH-QNN5	CH-HQER5	CH-GBR5	CH-GBT5
15	Pearson correlation	Lw_m, Az_deg, CPT_mean, CPT_median, CP_median, CP_mean, CPQ_range, CP_range	extEn	PC-QNN5	PC-HQER5	PC-GBR5	PC-GBT5
16	Boruta algorithm	CP_range, CPQ_range, CP_mean, CP_median, CP_sd, CPQ_mean, CI_median, CI_mean, CPQ_median	extQh	BO-QNN6	BO-HQER6	BO-GBR6	BO-GBT6
17	Chi-squared filter	CPQ_range, CP_range, CP_mean, CI_mean, CP_sd, CP_median, CI_median, CPQ_mean, CPQ_median	extQh	CH-QNN6	CH-HQER6	CH-GBR6	CH-GBT6
18	Pearson correlation	CPQ_range, CP_range, CP_sd, CI_median, CI_mean, CP_mean, CP_median, CPQ_mean, CPQ_median, CPQ_sd, CI_sd, CPT_mean, CI_range, CPT_median, dP_MPa	extQh	PC-QNN6	PC-HQER6	PC-GBR6	PC-GBT6

Notes: Features were selected based on a standardized weight threshold of $\geq$0.75, ensuring only the most influential predictors with strong statistical significance were retained for the modeling process.

Table 4. Performance metrics of surrogate QML models for tLife prediction comparing three feature selection methods and two quantum-based architectures.

Phase	Metrics	BO-QNN1	CH-QNN1	PC-QNN1	BO-HQER1	CH-HQER1	PC-HQER1
Train	MAE	2.105	2.005	2.472	1.473	1.422	1.428
	RMSE	3.122	3.191	4.073	2.427	2.303	2.519
	RSR	0.313	0.320	0.408	0.243	0.231	0.253
	dr	0.863	0.870	0.839	0.904	0.908	0.907
	R^2	0.901	0.896	0.831	0.940	0.946	0.935
Test	MAE	1.953	3.028	3.474	1.896	2.329	1.964
	RMSE	2.422	3.678	4.546	2.641	3.377	2.512
	RSR	0.226	0.344	0.425	0.247	0.316	0.235
	dr	0.892	0.832	0.807	0.895	0.871	0.891
	R^2	0.946	0.876	0.810	0.936	0.895	0.942

Notes: The units for MAE and RMSE are in year.

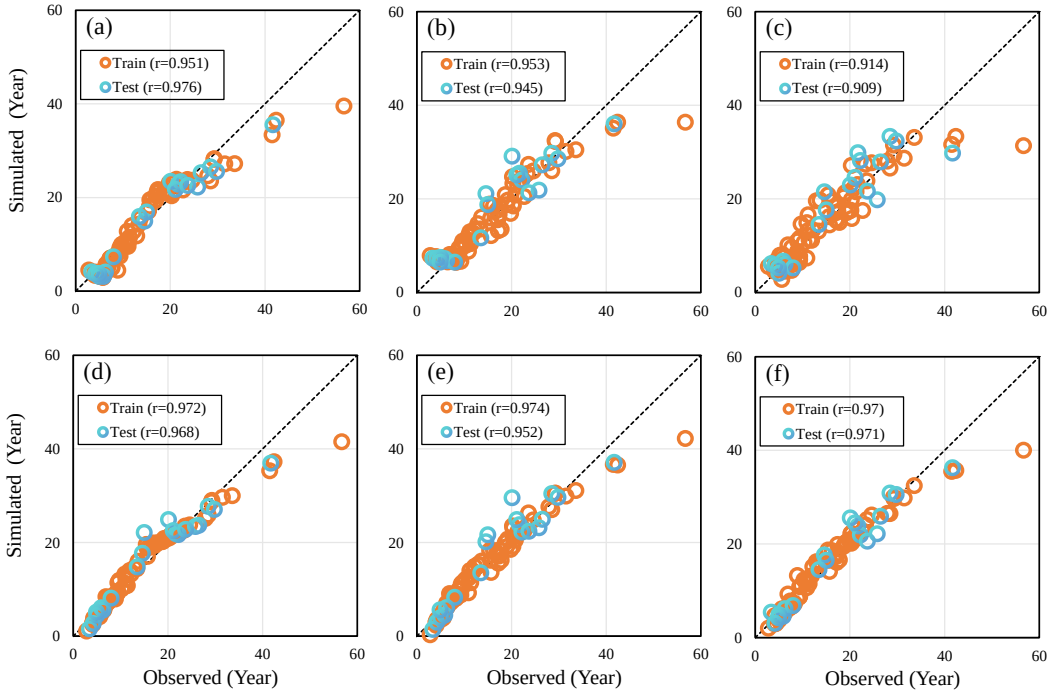

Fig. 3. Scatter plots comparing observed versus simulated tLife for six developed QML models. Each model was trained on 80 data samples and tested on 20 samples. The black diagonal line indicates a perfect prediction (1:1 line), and r represents the Pearson correlation coefficient.

results in the test phase. During the training phase, CH-HQER1 achieved the best overall performance with the lowest error metrics (MAE = 1.422 years, RMSE = 2.303 years, RSR = 0.231) and highest accuracy indicators (dr = 0.908, R^2 = 0.946), closely followed by BO-HQER1, suggesting that the HQER approach effectively captures the complex relationships between input features and tLife. The QNN models exhibited higher training errors but demonstrated better generalization in certain cases, with BO-QNN1 achieving the lowest test RMSE (2.422 years) and RSR (0.226), along with the highest test R^2 (0.946), indicating superior resistance to overfitting. The feature selection methodology significantly influenced model performance, with PC-QNN1 showing higher errors across both training and test sets. The relatively small degradation between training and test performance for most models validates the robustness of the quantum feature extraction approach and suggests that the models successfully learned generalizable patterns rather than memorizing training data. The mean absolute errors in the test set, ranging from 1.896 to 3.474 years, represent acceptable prediction accuracy, which shows that the proposed surrogate models can effectively replace computationally expensive NUFT simulations for rapid

Table 5. Performance metrics of developed QML models for iCO_2 prediction, comparing three feature selection methods and two quantum architectures.

Phase	Metrics	BO-QNN2	CH-QNN2	PC-QNN2	BO-HQER2	CH-HQER2	PC-HQER2
Train	MAE	0.698	0.996	1.358	0.473	0.606	0.592
	RMSE	0.865	1.243	1.678	0.632	0.815	0.825
	RSR	0.172	0.247	0.333	0.125	0.162	0.164
	dr	0.919	0.885	0.843	0.945	0.930	0.932
	R^2	0.970	0.938	0.888	0.984	0.974	0.973
Test	MAE	1.011	1.230	1.564	0.824	1.201	0.883
	RMSE	1.282	1.571	1.944	1.153	1.538	1.156
	RSR	0.235	0.288	0.356	0.211	0.282	0.212
	dr	0.892	0.868	0.832	0.912	0.871	0.905
	R^2	0.942	0.913	0.867	0.953	0.916	0.953

Notes: The MAE and RMSE units are in Mt.

tLife assessment.

The scatter plots of observed versus simulated tLife values are shown in Fig. 3. All six models demonstrate strong linear relationships between predictions and observations, with data points clustering tightly around the 1:1 line. The QNN models exhibit slightly more scattered predictions, especially PC-QNN1, which shows notable dispersion for both training and test sets (r = 0.914 and 0.909, respectively). In contrast, the HQER models display tighter clustering and achieve higher correlation coefficients compared to the QNN models for both train and test datasets (except the test section of BO-HQER1). The visual separation between training and test data points is minimal across all models, indicating robust generalization without significant overfitting, with test set correlations often matching or exceeding training correlations. The consistently high Pearson correlation values (r > 0.9) across all models confirm strong linear associations between predicted and observed values.

The QML-based models for iCO_2 prediction exhibit excellent performance with HQER architectures, demonstrating clear superiority over QNN implementations, particularly when combined with Boruta feature selection (Table 5). BO-HQER2 achieved exceptional training performance with the lowest error metrics across all measures (MAE = 0.473 Mt, RMSE = 0.632 Mt, RSR = 0.125) and highest accuracy indicators (dr = 0.945, R^2 = 0.984), maintaining this dominance in the test set with MAE of 0.824 Mt and R^2 of 0.953. The HQER models consistently outperformed their QNN counterparts by substantial margins, with training R^2 values exceeding 0.97 for all HQER variants compared to 0.888-0.97 for QNN models, suggesting that the ensemble approach with multiple classical regressors better captures the nonlinear dynamics of iCO_2 patterns.

The scatter plots for iCO_2 prediction (shown in Fig. 4) reveal exceptionally tight clustering around the 1:1 perfect prediction line across all six developed models. The HQER models consistently achieve higher Pearson correlation coefficients than their QNN counterparts, with BO-HQER2 attaining the highest overall correlations (r = 0.992 for training, r = 0.977 for test), indicating near-perfect linear relationships between predicted and observed values. All models show remarkable consistency across the 5-25 Mt range with minimal scatter, suggesting that the quantum feature extraction effectively captures the relatively straightforward relationship between inputs and outputs of QML models. The QNN models, while showing slightly lower correlations, still maintain impressive performance with all variants exceeding r = 0.93 for both datasets, with BO-QNN2 achieving particularly strong results (r = 0.985 training, r = 0.972 test). A notable characteristic across all models is the minimal degradation between training and test correlations, with differences typically around 0.02, confirming robust generalization and absence of overfitting.

The performance metrics of the developed surrogate QML models for eCO_2 prediction are listed in Table 6. BO-HQER3 resulted as the best model with training metrics (MAE = 0.277 Mt, RMSE = 0.361 Mt, RSR = 0.119, dr = 0.947, R^2 = 0.986) and maintained this dominance in the test section (MAE = 0.501 Mt, RMSE = 0.73 Mt, R^2 = 0.951), demonstrating stability and generalization capability for eCO_2 prediction. In general, all HQER variants achieve training R^2 values above 0.976 compared to 0.889-0.965 for QNN models, suggesting that the HQER approach more effectively captures the complex patterns of eCO_2. The feature selection via Pearson correlation-based models with expanded feature sets achieves strong performance in HQER (test R^2 = 0.943) but suffers in QNN architecture, indicating that HQER's ensemble structure better leverages diverse feature information. The relatively modest increase in test errors, with MAE ranging from 0.501 to 0.862 Mt, confirms the developed models' ability to predict eCO_2 as surrogate models accurately.

The scatter plots for eCO_2 prediction demonstrate strong relationships between observed and simulated values (shown in Fig. 5), with all models achieving Pearson correlation coefficients exceeding 0.94. The HQER models consistently

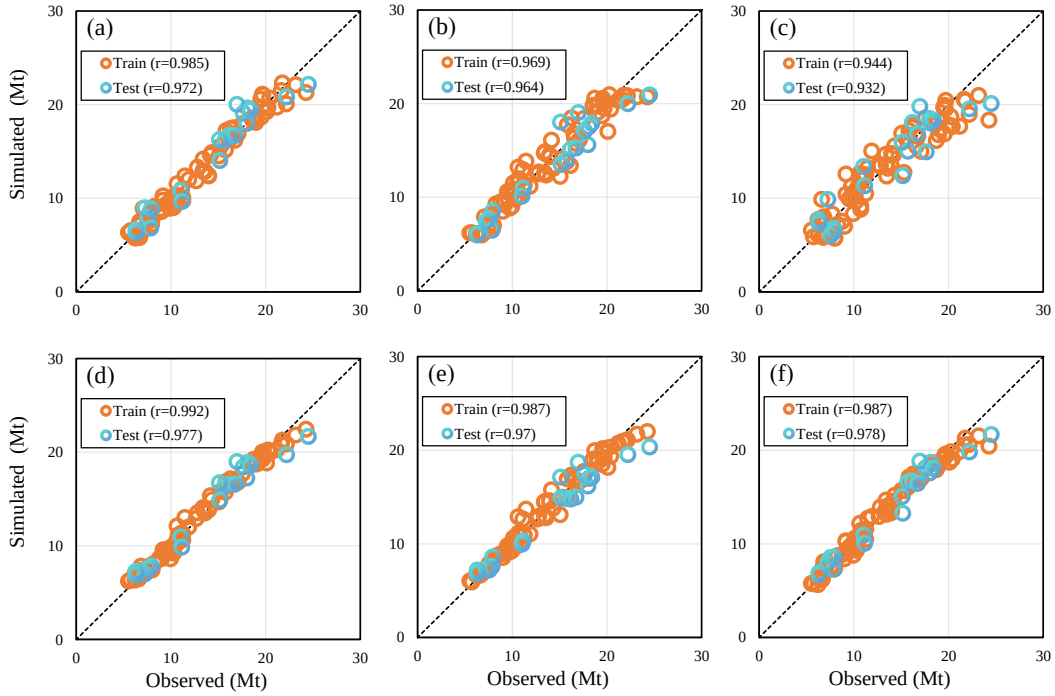

Fig. 4. Scatter plots comparing observed versus simulated iCO2 for BO-QNN2 (a), CH-QNN2 (b), PC-QNN2 (c), BO-HQER2 (d), CH-HQER2 (e), and PC-HQER2 (f) models. Each model was trained on 80 data samples and tested on 20 samples. The black diagonal line indicates perfect prediction (1:1 line) and r represents the Pearson correlation coefficient.

Table 6. Performance metrics of QML models for eCO_2 prediction comparing three feature selection methods and two quantum architectures.

Phase	Metrics	BO-QNN3	CH-QNN3	PC-QNN3	BO-HQER3	CH-HQER3	PC-HQER3
Train	MAE	0.453	0.590	0.765	0.277	0.360	0.350
	RMSE	0.559	0.709	0.999	0.361	0.464	0.458
	RSR	0.185	0.234	0.331	0.119	0.154	0.151
	dr	0.913	0.887	0.854	0.947	0.931	0.933
	R^2	0.965	0.944	0.889	0.986	0.976	0.977
Test	MAE	0.740	0.806	0.862	0.501	0.780	0.598
	RMSE	0.906	1.003	1.162	0.730	0.986	0.794
	RSR	0.266	0.295	0.342	0.215	0.290	0.234
	dr	0.873	0.862	0.852	0.914	0.866	0.897
	R^2	0.925	0.908	0.877	0.951	0.911	0.943

Notes: The MAE and RMSE units are in Mt.

outperform their QNN counterparts in terms of correlation strength, with BO-HQER3 achieving the highest correlations (r = 0.989 for train and r = 0.979 for test phases), demonstrating near-perfect alignment along the 1:1 line. In addition, all QNN models maintain impressive correlations, with BO-QNN3 achieving r = 0.983 for the training and r = 0.972 for testing sections. The HQER models display almost consistent performance across all feature selection methods, with training correlations ranging from 0.989 to 0.993 and test correlations from 0.971 to 0.979, indicating that the ensemble approach robustly integrates different feature sets to maintain high eCO_2 prediction accuracy.

The QML models for sCO_2 prediction exhibit strong performance (Table 7) with BO-HQER4 achieving the best accuracy across all metrics. BO-HQER4 dominated both training (MAE = 0.276 Mt, RMSE = 0.377 Mt, RSR = 0.183, dr = 0.921, R^2 = 0.966) and testing phases (MAE = 0.422 Mt, RMSE = 0.496 Mt, R^2 = 0.941), with the minimal R^2 degradation of only 0.025 indicating robust learning of the fundamental relationships between inputs and outputs dataset in HQER models for sCO_2 prediction. The HQER architectures consistently outperformed QNN models by substantial

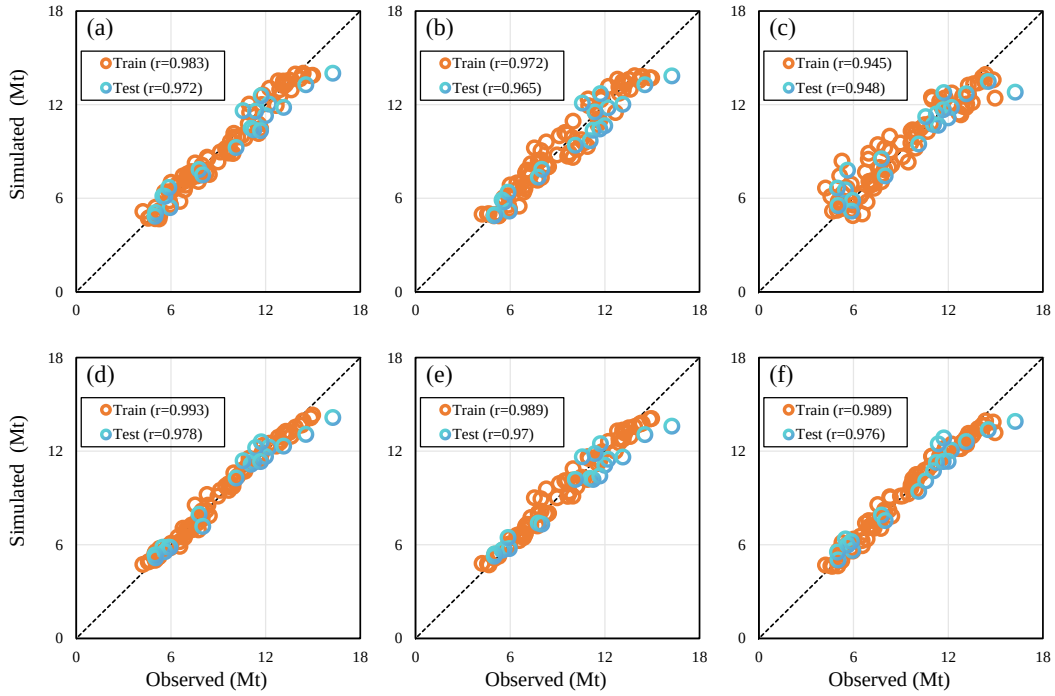

Fig. 5. Scatter plots comparing observed versus simulated eCO2 for BO-QNN3 (a), CH-QNN3 (b), PC-QNN3 (c), BO-HQER3 (d), CH-HQER3 (e), and PC-HQER3 (f). Each model was trained on 80 data samples and tested on 20 samples. The black diagonal line indicates perfect prediction (1:1 line) and r represents the Pearson correlation coefficient.

Table 7. Performance metrics of developed QML models for sCO_2 prediction, comparing three feature selection methods and two quantum architectures.

Phase	Metrics	BO-QNN4	CH-QNN4	PC-QNN4	BO-HQER4	CH-HQER4	PC-HQER4
Train	MAE	0.409	0.542	0.520	0.276	0.337	0.313
	RMSE	0.531	0.693	0.691	0.377	0.452	0.443
	RSR	0.257	0.335	0.334	0.183	0.219	0.214
	dr	0.883	0.845	0.851	0.921	0.904	0.910
	R^2	0.933	0.886	0.887	0.966	0.952	0.954
Test	MAE	0.519	0.531	0.774	0.422	0.491	0.544
	RMSE	0.598	0.720	0.953	0.496	0.640	0.732
	RSR	0.286	0.345	0.456	0.237	0.306	0.350
	dr	0.852	0.848	0.779	0.880	0.860	0.845
	R^2	0.914	0.875	0.781	0.941	0.901	0.871

Notes: The MAE and RMSE units are in Mt.

margins, with training R^2 values ranging from 0.952 to 0.966 for HQER compared to 0.886-0.933 for QNN, suggesting that the ensemble approach more effectively captures the complex process of sCO_2. Chi-squared and Pearson correlation feature selection approaches achieved comparable training performance in HQER architectures ($R^2 > 0.95$) but showed divergent test results, with PC-HQER4 experiencing larger degradation ($R^2 = 0.871$) compared to CH-HQER4 ($R^2 = 0.901$), indicating that the minimal feature set may provide better generalization for sCO_2 prediction. The QNN models showed greater sensitivity to feature selection, with PC-QNN4 suffering significant test performance degradation ($R^2 = 0.781$) despite reasonable training metrics, suggesting that the expanded feature set introduced noise that the QNN architecture could not effectively filter.

The scatter plots for sCO_2 prediction reveal strong correlations between observed and simulated sCO_2 values (shown in Fig. 6). The HQER models demonstrate superior performance, with BO-HQER4 achieving the highest correlations ($r = 0.984$ for training, $r = 0.97$ for testing phases), showing exceptional alignment along the 1:1 prediction line. All models exhibit tighter clustering in the lower storage range (2.5-5

Mt) with increased dispersion at higher values (> 7.5 Mt), suggesting that predicting larger amounts of sCO_2 becomes more challenging. The QNN models, while showing slightly lower correlations, still maintain strong predictive capability, with BO-QNN4 achieving impressive performance (r = 0.969 training and r = 0.958 testing phases). A distinct pattern emerges where Pearson correlation-based models show the largest train-test correlation gaps (PC-QNN4: 0.946 to 0.927; PC-HQER4: 0.978 to 0.933).

Table 8 presents the performance metrics of the developed surrogate QML models for extEn prediction. The results show outstanding predictive accuracy, with BO-HQER5 delivering exceptional performance that outperforms all other configurations. BO-HQER5 attained outstanding training metrics (MAE = 0.116 PJ, RMSE = 0.151 PJ, RSR = 0.122, dr = 0.946, R^2 = 0.985) and maintained superior test performance (MAE = 0.212 PJ, RMSE = 0.307 PJ, R^2 = 0.95), with the modest R^2 degradation of 0.035 confirming robust generalization despite the complex interplay between thermal transport, fluid flow, and reservoir dynamics governing energy extraction. The HQER architectures consistently outperformed QNN models with training R^2 values exceeding 0.974 compared to 0.89-0.961 for QNN variants, demonstrating that the HQER more effectively captures the extEn process. Feature selection revealed intriguing patterns where PC-HQER5, despite including additional features beyond the core geometric parameters, achieved the second-best test R^2 of 0.942, suggesting that extEn prediction benefits from incorporating production statistics when properly integrated through ensemble methods. The QNN models showed reasonable performance with BO-QNN5 achieving test R^2 of 0.915, resulted as the best QNN-base model for extEn prediction.

Fig. 7 shows the scatter plots for extEn prediction that demonstrate strong correlations between observed and simulated extEn values, with all models achieving Pearson correlation coefficients exceeding 0.93. BO-HQER5 exhibits the strongest performance with outstanding correlations (r = 0.993 for training and r = 0.978 for testing phases), showing near-perfect alignment along the 1:1 prediction line. The HQER models consistently outperform their QNN counterparts, with all HQER variants achieving training correlations equal to or above 0.988 compared to 0.945-0.982 for QNN models.

Table 9 presents performance metrics of the developed QML models for extQh prediction. Boruta and Chi-squared feature selection methods produced identical results within each architecture, suggesting convergence on the same critical production and heat flux statistics, while demonstrating a performance gap between HQER and QNN architectures among all target variables. BO-HQER6 and CH-HQER6 achieved identical exceptional training performance (MAE = 0.196 MW, RMSE = 0.286 MW, RSR = 0.08, dr = 0.967, R^2 = 0.994) and maintained this equivalence in testing (MAE = 0.419 MW, RMSE = 0.993 MW, R^2 = 0.95), indicating that both feature selection methods identified the same optimal subset of production-related features. The HQER-based model shows superiority over the QNN-based model for extQh prediction, with training R^2 of 0.994 versus 0.905-0.915 and test R^2 of 0.95 versus 0.795-0.901. PC-QNN6 achieved notably better test performance (R^2 = 0.901) compared to BO/CH-QNN6 (R^2 = 0.795), indicating that the additional features selected by Pearson correlation could provide better regularization for the QNN architecture.

Fig. 8 shows the scatter plots for extQh prediction via the developed QML models. The HQER-based models demonstrate exceptional predictive accuracy with remarkably tight clustering along the 1:1 line, achieving r = 0.997 for the train sections of BO/CH-HQER6 and r = 0.996 for the train section of PC-HQER6. Both models showed slightly lower r-values in the test section compared to the corresponding values in the training section. The superior performance of HQER models maintains test correlations above 0.96 compared to 0.90-0.95 for QNN variants. The identical visual patterns and correlations for BO and CH methods within each architecture type provide evidence that both algorithms identified the same input features for developed models.

The comparative performance of the developed quantum-based and classical baseline models is presented in Supplementary E of the supplementary information. The results of the multi-objective optimization are provided in Supplementary F, and the limitations and future work are discussed in Supplementary G of the supplementary information.

4. Conclusion

The optimization of CO_2 plume geothermal systems represents a critical technological frontier for achieving simultaneous carbon sequestration and renewable energy production, yet conventional numerical modeling approaches require prohibitive computational resources that severely limit design optimization and uncertainty quantification capabilities essential for commercial deployment. This study addresses this fundamental computational barrier through the application of QML to CPG system optimization, demonstrating that QNNs and HQER can serve as accurate surrogate models for complex multiphase flow and heat transport simulations. This study successfully demonstrated the transformative potential of QML for accelerating CPG system optimization by developing a novel hybrid NUFT-QML framework that achieves computational speedup while maintaining prediction accuracy across all performance metrics. Each NUFT simulation requires approximately 1 hour of computational time, whereas the developed surrogate models significantly reduce computation time. Specifically, the QNN model requires about 163 to 562 seconds, and the HQER model takes approximately 18 to 41 seconds, depending on the number of input features used in the model. The comprehensive evaluation of two quantum architectures (QNN and HQER) combined with three feature selection methods (Boruta, Chi-squared, Pearson correlation) revealed that HQER consistently outperformed pure QNN, achieving exceptional accuracy with $R^2 > 0.95$ for most target variables, particularly when paired with Boruta feature selection method. The developed surrogate QML models demonstrated remarkable generalization capability with minimal train-test degradation, successfully capturing complex nonlinear relationships between reservoir parameters and system performance metrics, including extEn, sCO_2,

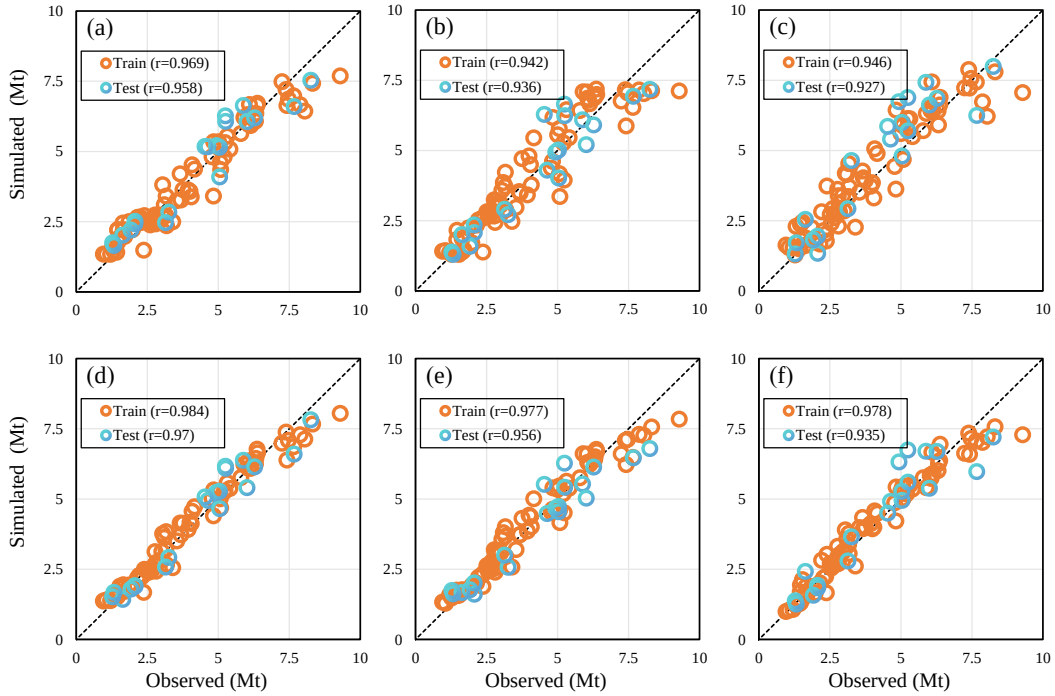

Fig. 6. Scatter plots comparing observed versus simulated sCO2 for BO-QNN4 (a), CH-QNN4 (b), PC-QNN4 (c), BO-HQER4 (d), CH-HQER4 (e), and PC-HQER4 (f) models. Each model was trained on 80 data samples and tested on 20 samples. The black diagonal line indicates a perfect prediction (1:1 line) and r represents the Pearson correlation coefficient.

Table 8. Performance metrics of QML models for extEn prediction comparing three feature selection methods and two quantum architectures.

Phase	Metrics	BO-QNN5	CH-QNN5	PC-QNN5	BO-HQER5	CH-HQER5	PC-HQER5
Train	MAE	0.186	0.251	0.311	0.116	0.155	0.145
	RMSE	0.243	0.301	0.410	0.151	0.198	0.191
	RSR	0.195	0.242	0.329	0.122	0.160	0.153
	dr	0.913	0.883	0.855	0.946	0.928	0.933
	R^2	0.961	0.941	0.890	0.985	0.974	0.976
Test	MAE	0.289	0.338	0.359	0.212	0.336	0.247
	RMSE	0.399	0.421	0.485	0.307	0.422	0.329
	RSR	0.284	0.300	0.345	0.218	0.300	0.234
	dr	0.880	0.860	0.851	0.912	0.861	0.897
	R^2	0.915	0.905	0.874	0.950	0.905	0.942

Notes: The units of MAE and RMSE are in PJ.

tLife, and extQh. Comparative analysis revealed that quantum-enhanced models consistently outperform or match classical baselines while requiring substantially fewer input features, demonstrating clear quantum advantages in data efficiency and feature economy. The integration of MFO for single-objective and NSGA-II for multi-objective optimization enabled rapid exploration of design spaces in northern Oman, converging to robust optimal configurations with injection pressure around 5 MPa and well spacing near 970 m that naturally balance energy extraction, carbon sequestration, and operational longevity. The practical implications of this research extend beyond computational acceleration, establishing QML as a viable technology for real-time reservoir management and rapid techno-economic assessment of CPG systems, which is important for commercial deployment. The convergence of multiple optimization scenarios to similar optimal solutions validates the robustness of the identified configurations and suggests fundamental trade-offs in CPG system design that transcend specific objective formulations.

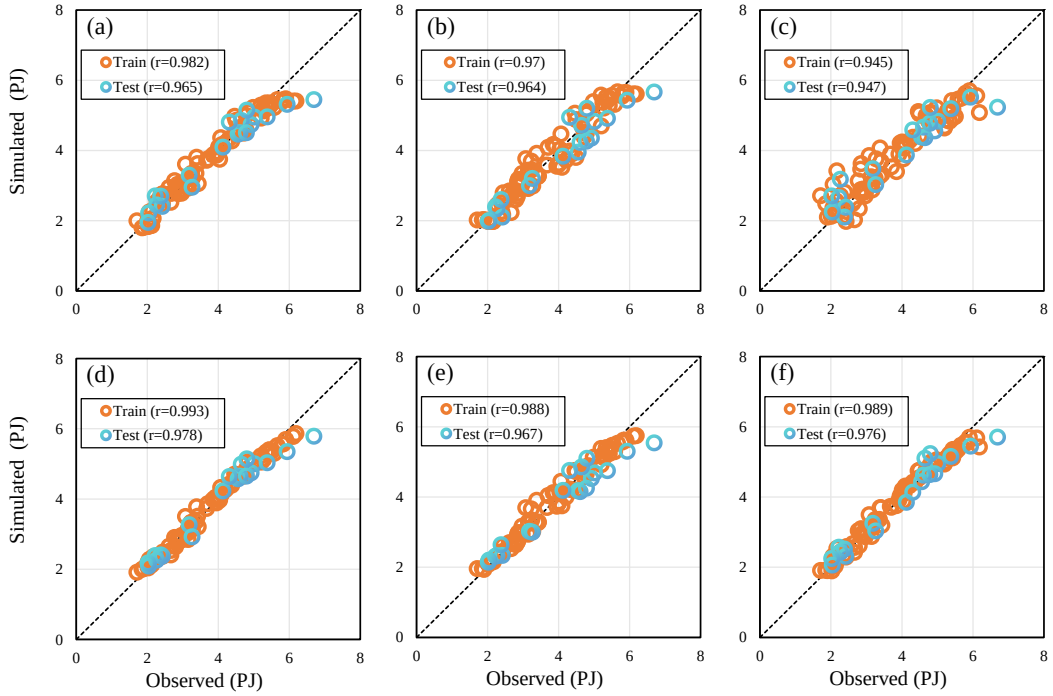

Fig. 7. Scatter plots compare observed versus simulated extEn for BO-QNN5 (a), CH-QNN5 (b), PC-QNN5 (c), BO-HQER5 (d), CH-HQER5 (e), and PC-HQER5 (f) models. Each model was trained on 80 data samples and tested on 20 samples. The black diagonal line indicates a perfect prediction (1:1 line) and r represents the Pearson correlation coefficient.

Table 9. Performance metrics of QML models for extQh prediction comparing three feature selection methods and two quantum architectures.

Phase	Metrics	BO-QNN6	CH-QNN6	PC-QNN6	BO-HQER6	CH-HQER6	PC-HQER6
Train	MAE	0.846	0.846	0.868	0.196	0.196	0.201
	RMSE	1.037	1.037	1.099	0.286	0.286	0.316
	RSR	0.289	0.289	0.307	0.080	0.080	0.088
	dr	0.856	0.856	0.853	0.967	0.967	0.966
	R^2	0.915	0.915	0.905	0.994	0.994	0.992
Test	MAE	1.123	1.123	1.028	0.419	0.419	0.493
	RMSE	2.007	2.007	1.395	0.993	0.993	1.262
	RSR	0.441	0.441	0.307	0.218	0.218	0.278
	dr	0.848	0.848	0.861	0.943	0.943	0.933
	R^2	0.795	0.795	0.901	0.950	0.950	0.919

Notes: The units of MAE and RMSE are in megawatts (MW).

Acknowledgements

The study is supported by grants #CL/SQU-IGGCAS/WRC/23/01, #IG/DVC/WRC/24/01 from Sultan Qaboos University (SQU), Oman. SQU group DR/RG/17's is also appreciated.

Supplementary file

https://doi.org/10.46690/ager.2025.11.04

Conflict of interest

The authors declare no competing interest.

References

Antoneas, G., Koronaki, I. Geothermal Solutions for Urban Energy Challenges: A Focus on CO_2 Plume Geothermal

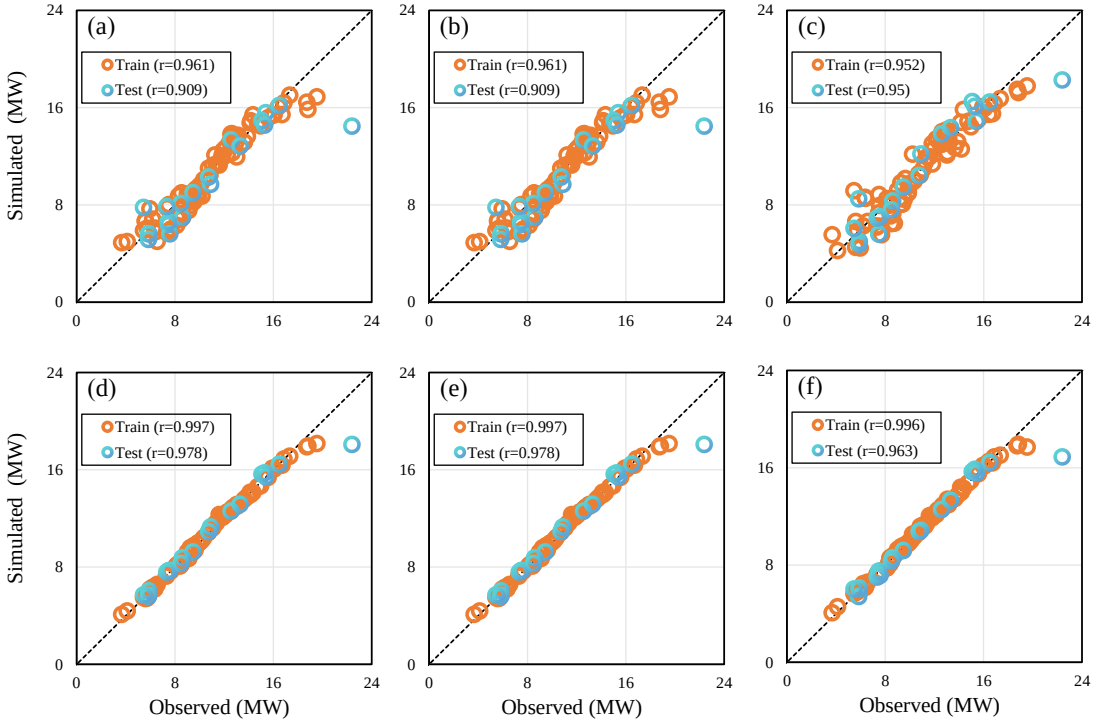

Fig. 8. Scatter plots comparing observed versus simulated extQh for BO-QNN6 (a), CH-QNN6 (b), PC-QNN6 (c), BO-HQER6 (d), CH-HQER6 (e), and PC-HQER6 (f) models. Each model was trained on 80 data samples and tested on 20 samples. The black diagonal line indicates a perfect prediction (1:1 line) and r represents the Pearson correlation coefficient.

Systems. Energies, 2024, 17(2): 294.

Bui, M., S. Adjiman, C., Bardow, A., J. et al. Carbon capture and storage (CCS): the way forward. Energy & Environmental Science, 2018, 11(5): 1062-1176.

Buscheck, T. A., Sun, Y., Chen, M., et al. Active CO_2 reservoir management for carbon storage: Analysis of operational strategies to relieve pressure buildup and improve injectivity. International Journal of Greenhouse Gas Control, 2012, 6: 230-245.

Buscheck, T. A., Bielicki, J. M., Edmunds, T. A., et al. Multifluid geo-energy systems: Using geologic CO_2 storage for geothermal energy production and grid-scale energy storage in sedimentary basins. Geosphere, 2016, 12(3): 678-696.

Chen, M., Al-Maktoumi, A., Mahdi Rajabi, M., et al. Evaluation of CO_2 sequestration and circulation in fault-bounded thin geothermal reservoirs in North Oman using response surface methods. Journal of Hydrology, 2021, 598: 126411.

Chen, M., Al-Saidi, A., Al-Maktoumi, A., et al. The impact of geological heterogeneity on horizontal well-triplet performance in CO_2-circulated geothermal reservoirs. Advances in Geo-Energy Research, 2022, 6(3): 192-205.

Chen, M., Reza Nikoo, M., Al-Maktoumi, A., et al. The impact of geological heterogeneity on coupled CO_2 storage and geothermal extraction in inclined reservoirs. Journal of Hydrology, 2023, 617: 128950.

Chen, W. The Application of Different Surrogate Models in Engineering Predictions. Applied and Computational Engineering, 2024, 80: 87-93.

Dai, Z., Middleton, R., Viswanathan, H., et al. An Integrated Framework for Optimizing CO_2 Sequestration and Enhanced Oil Recovery. Environmental Science & Technology Letters, 2014, 1(1): 49-54.

Ezekiel, J., Ebigbo, A., Adams, B. M., et al. Combining natural gas recovery and CO_2-based geothermal energy extraction for electric power generation. Applied Energy, 2020, 269: 115012.

Fleming, M. R., Adams, B. M., Randolph, J. B., et al. High Efficiency and Large-Scale Subsurface Energy Storage with CO_2. In 43rd Workshop on Geothermal Reservoir Engineering, Stanford, CA. 2018.

Fraces, C. G., Tchelepi, H. Physics informed deep learning for flow and transport in porous media. Paper SPE 203934 Presented at the SPE Reservoir Simulation Conference, On-Demand. 26 October, 2021.

Garapati, N., Randolph, J. B., Saar, M. O. Brine displacement by CO_2, energy extraction rates, and lifespan of a CO_2-limited CO_2-Plume Geothermal (CPG) system with a horizontal production well. Geothermics, 2015, 55: 182-194.

Li, F., Guo, X., Qi, X., et al. A Surrogate Model-Based Optimization Approach for Geothermal Well-Doublet Placement Using a Regularized LSTM-CNN Model and Grey Wolf Optimizer. Sustainability, 2025, 17(1): 266.

Loschetter, A., Kervévan, C., Stead, R., et al. Integrating geothermal energy and carbon capture and storage technologies: A review. Renewable and Sustainable Energy

Reviews, 2025, 210: 115179.

Mac Dowell, N., Fennell, P. S., Shah, N., et al. The role of CO_2 capture and utilization in mitigating climate change. Nature Climate Change, 2017, 7(4): 243-249.

Malik, M. M. A Hierarchy of Limitations in Machine Learning. ArXiv Preprint ArXiv: 2002.05193, 2020.

Metz, B., Davidson, O., De Coninck, H. C., et al. IPCC special report on carbon dioxide capture and storage. Cambridge: Cambridge University Press, 2005.

Mirjalili, S. Moth-flame optimization algorithm: A novel nature-inspired heuristic paradigm. Knowledge-Based Systems, 2015, 89: 228-249.

Ng, C. S. W., Nait Amar, M., Jahanbani Ghahfarokhi, A., et al. A Survey on the Application of Machine Learning and Metaheuristic Algorithms for Intelligent Proxy Modeling in Reservoir Simulation. Computers & Chemical Engineering, 2023, 170: 108107.

Nikravesh, M., Adams, R. D., Levey, R. A. Soft computing: tools for intelligent reservoir characterization (IRESC) and optimum well placement (OWP). Journal of Petroleum Science and Engineering, 2001, 29(3): 239-262.

Norouzi, A. M., Babaei, M., Han, W. S., et al. CO_2-plume geothermal processes: A parametric study of salt precipitation influenced by capillary-driven backflow. Chemical Engineering Journal, 2021, 425: 130031.

Norouzi, A.M., Gluyas, J., Babaei, M. CO_2-plume geothermal in fluvial formations: A 2D numerical performance study using subsurface metrics and upscaling. Geothermics, 2022, 99, 102287.

Pruess, K. On production behavior of enhanced geothermal systems with CO_2 as working fluid. Energy Conversion and Management, 2008, 49(6): 1446-1454.

Rajabi, M. M., Chen, M., Bozorgpour, A., et al. Stochastic Techno-economic Analysis of CO_2-circulated Geothermal Energy Production in a Closed Reservoir System. Geothermics, 2021, 96: 102202.

Rajabi, M. M., Chen, M., Reza Hajizadeh Javaran, M., et al. Probabilistic net present value analysis for designing techno-economically optimal sequential CO_2 sequestration and geothermal energy extraction. Journal of Hydrology, 2022, 612: 128237.

Randolph, J. B., Saar, M. O. Combining geothermal energy capture with geologic carbon dioxide sequestration. Geophysical Research Letters, 2011, 38(10): L10401.

Saikia, P., Baruah, R. D., Singh, S. K., et al. Artificial Neural Networks in the domain of reservoir characterization: A review from shallow to deep models. Computers & Geosciences, 2020, 135: 104357.

Semler, P., Weiser, M. Adaptive Gaussian process regression for efficient building of surrogate models in inverse problems. Inverse Problems, 2023, 39(12): 125003.

Shen, C., Appling, A. P., Gentine, P., et al. Differentiable modelling to unify machine learning and physical models for geosciences. Nature Reviews Earth & Environment, 2023, 4(8): 552-567.

Teixeira, A. F., Secchi, A. R. Machine learning models to support reservoir production optimization. IFAC-PapersOnLine, 2019, 52(1): 498-501.

Titus, K. A., Dempsey, D. E., Peer, R. A. M. Carbon negative geothermal: Theoretical efficiency and sequestration potential of geothermal-BECCS energy cycles. International Journal of Greenhouse Gas Control, 2023, 122: 103813.

Wang, J., Zhao, Z., Liu, G., et al. A robust optimization approach of well placement for doublet in heterogeneous geothermal reservoirs using random forest technique and genetic algorithm. Energy, 2022, 254: 124427.

Wen, G., Hay, C., Benson, S. M. CCSNet: A deep learning modeling suite for CO_2 storage. Advances in Water Resources, 2021, 155: 104009.

Williams, G. A., Chadwick, R. A. Influence of reservoir-scale heterogeneities on the growth, evolution and migration of a CO_2 plume at the Sleipner Field, Norwegian North Sea. International Journal of Greenhouse Gas Control, 2021, 106: 103260.

Ye, Z., Wang, J. G., Yang, J. A multi-objective optimization approach for a fault geothermal system based on response surface method. Geothermics, 2024, 117: 102887.

Zhong, C., Xu, T., Gherardi, F., Yuan, Y. Comparison of CO_2 and water as working fluids for an enhanced geothermal system in the Gonghe Basin, northwest China. Gondwana Research, 2023, 122: 199-214.

Zhou, C., Zhang, H., Chang, Q., et al. An adaptive ensemble of surrogate models based on hybrid measure for reliability analysis. Structural and Multidisciplinary Optimization, 2022, 65(1): 1-18.